https://dx.doi.org/10.1016/j.matchar.2021.111687

Atomistic study of Al partitioning and its influence on nanoscale precipitation of Cu-rich nanocluster-strengthened steels

B.C. Zhou[a,b], C.Y. Yu[c], S. Qiu[a,b], T. Yang[d], J.H. Luan[d], X.Q. Xu[e,f], Z.C. Luo[g], Z.B. Jiao[a,b,*]

[a] *Department of Mechanical Engineering, The Hong Kong Polytechnic University, Hong Kong, China*

[b] *The Hong Kong Polytechnic University Shenzhen Research Institute, Shenzhen, China*

[c] *College of Physics and Optoelectronic Engineering, Shenzhen University, Shenzhen 518060, China*

[d] *Department of Materials Science and Engineering, City University of Hong Kong, Hong Kong, China*

[e] *School of Mechanical Engineering, Tongling University, Tongling 244000, China*

[f] *Key Laboratory of Construction Hydraulic Robots of Anhui Higher Education Institutes, Tongling University, Tongling 244000, China*

[g] *Institute of Materials and Processing, Guangdong Academy of Science, Guangzhou 510000, China*

* *Corresponding authors: zb.jiao@polyu.edu.hk*

Abstract

The intrinsic partitioning behavior of Al and its influence on the nanoscale precipitation of Cu-rich nanocluster-strengthened steels were investigated by using atom probe tomography (APT) and first-principles calculations. The APT results reveal that Al partitions to Cu-rich nanoclusters, which results in a slight decrease in the volume fraction of the nanoclusters. The first-principles calculations indicate that the Al substitution in body-centered cubic (bcc) Cu is more energetically favorable as compared with that in bcc Fe. In addition, the Al partitioning has no significant influence on the chemical driving force and interfacial energy but slightly increases the strain energy for nucleation, thereby increasing the critical energy for the formation of Cu-rich nanoclusters. As a result, the nanoscale Cu precipitation is slightly inhibited in the Al-containing ferritic steels. In addition, the effects of Al on the precipitation strengthening response were quantitatively evaluated, and the results indicate that the degree

of precipitation strengthening depends majorly on the combined effect of cluster size and inter-cluster spacing.

Keywords: Cu-rich nanocluster; Al partitioning; nanoscale precipitation; ferritic steel

1. Introduction

Cu-rich nanocluster-strengthened low-carbon steels have received considerable attention in terms of both fundamental research and potential technological applications in the automotive, shipbuilding, and construction industries [1-6]. Considerable effort has been devoted to understanding the precipitation behavior and strengthening mechanisms of Cu-rich nanoclusters in high-strength steels [7-11]. It has been documented that body-centered cubic (bcc) Cu-rich nanoclusters form coherently with the bcc Fe matrix at an early stage of precipitation, and prolonged annealing leads to the transformation from the coherent bcc structure to the semi-coherent 9R twinned structure, and finally to the incoherent face-centered cubic (fcc) structure [12-14]. In addition, notable segregation of solute elements to the nanoclusters and interfaces were often observed, which was reported to have a significant impact on the Cu precipitation and the corresponding strengthening response [15-17]. For example, Ni was found to be energetically favorable to segregate at the interface between the Cu-rich nanoclusters and matrix, the segregation of which effectively decreases the interfacial energy of Cu-rich nanoclusters, thereby promoting the nucleation of Cu-rich nanoclusters and enhancing their strengthening effect [18-22]. When Ni and Al are co-added to Fe-Cu-based steels, the co-segregation of Ni and Al at the interface between the Cu-rich nanoclusters and matrix can be observed, which often leads to the heterogeneous nucleation of NiAl precipitates at the Cu-nanocluster/matrix interface [21,23,24]. It is worthy to point out that Al has a strong affinity to Ni, which can be reflected from the large negative heat of mixing between Ni and Al (-22 kJ/mol) [25-27], and thus, the partitioning behavior of Al might be influenced by the

interaction between Ni and Al atoms in the multicomponent Fe-Cu-Ni-Al-based steels. Recently, the partitioning behavior of Al in Fe-Cu-based steels was studied by simulations, but the findings are debated by different investigations; some simulations suggest that Al is energetically favorable to segregate at the interface between the Cu-rich nanoclusters and matrix [28-30], while some others suggest that Al tends to partition to the core of Cu-rich nanoclusters [31]. Furthermore, Al is known as a ferrite stabilizer and has a large solubility in bcc Fe [32]. A strong partitioning of Al to the bcc Fe matrix was observed in some precipitation-hardened ferritic steels [33,34]. To date, a thorough investigation of the intrinsic partitioning behavior of Al in Cu-rich nanocluster-strengthened ferritic steels has yet to be undertaken, and the mechanisms for the influence of Al partitioning on the nanoscale Cu precipitation remain unclear.

The aim of this study is to systematically investigate the intrinsic partitioning behavior of Al and its influence on the nanoscale precipitation of Cu-rich nanocluster-strengthened steels through a combination of experimental and simulation approaches. Because Cu-rich nanoclusters usually have a coherent relation to the magnetic Fe-based matrix in the early stage of precipitation, it is difficult to quantitatively characterize the elemental partitioning and precipitate properties by using transmission electron microscopy. Alternatively, atom probe tomography (APT) provides three-dimensional atom maps showing the elemental distribution at the atomic scale. Thus, APT was used to study the partitioning behavior of Al in Cu-rich nanocluster-strengthened steels in this study. Specifically, to eliminate the influence of Ni and other solute elements on the intrinsic partitioning behavior of Al, three model alloys with compositions of Fe-2Cu-xAl (x = 0, 0.5, and 1 wt.%) were used for this research. In addition, first-principles calculations were performed to gain insights into the lattice occupancy of Al in the bcc Fe-Cu system and the interaction mechanisms between the Al partitioning and Cu-rich nanoclusters.

2. Experimental

The three steels with the compositions of Fe-2Cu, Fe-2Cu-0.5Al, and Fe-2Cu-1Al (wt.%) were arc-melted using elemental ingredients with a purity of above 99.9 wt.% and cast into a copper mold with a cavity of 50 × 15 × 3 mm^3. For simplicity, these steels are hereafter referred to as 0Al, 0.5Al, and 1Al steels. The as-cast ingots were cold-rolled with a thickness reduction of 67% and solution-treated at 1150 °C for 3 min, followed by water quenching, and then aged at 550 °C for various periods of time.

Hardness measurements were conducted using a Vickers hardness tester with a load of 1 kN and a dwell time of 15 s, and at least 8 indents for each specimen were measured to obtain an average value. Tensile specimens with a gauge length of 12.5 mm and a cross-section of 3.2 × 1 mm^2 were cut by electro-discharge machining and polished with up to 2000-grit SiC paper, and tensile properties were tested by using an MTS tensile test machine at a strain rate of 10^{-3} s^{-1}. Samples for SEM observations were mechanically polished using 0.05 μm alumina particles until obtaining a mirror-like surface. The average grain size was measured via a linear intercept method.

Needle-shaped specimens for APT experiments were prepared by lift-out and annular milling in a FEI Scios focused-ion beam/scanning electron microscope. APT experiments were performed in a LEAP^{TM} 5000 XR in voltage mode, with a specimen temperature of 50 K, a pulse repetition rate of 200 kHZ, and a pulse fraction of 0.2. Image Visualization and Analysis Software version 3.8 was used for three-dimensional reconstruction, compositional analyses, and the creation of iso-concentration surfaces.

First-principles calculations were performed in the frame-work of density functional theory using the Vienna *ab initio* Simulation Package (VASP) [35-37]. Three-dimensional periodic supercells with 4 × 4 × 4 and 3 × 3 × 3 unit cells were built to determine the total supercell energies. A plane-wave energy cutoff of 400 eV was used in all calculations.

Equilibrium cell volumes and all internal atomic positions of the supercells were fully relaxed until convergence with a total energy tolerance of 10^{-4} eV.

3. Results

Microhardness measurements were conducted to evaluate the effect of Al on the precipitation hardening behavior of the Fe-2Cu-*x*Al steels during the isothermal aging. The Vickers hardness values of the 0Al, 0.5Al, and 1Al steels are shown in Fig. 1 as a function of aging time. The three steels have similar hardness values in the as-quenched condition, and their hardness profiles display a similar trend of aging hardening. For the three steels, the hardness increases rapidly from ~130 HV in the as-quenched condition to ~ 220 HV in the 15-min aged condition and reaches peak values of ~230 HV in the 1-h aged condition, resulting in a pronounced hardness increment of approximately 110 HV. Further aging leads to a gradual decrease in the hardness, indicating an overaging effect.

Representative SEM microstructures of the 0Al, 0.5Al, and 1Al steels in the as-quenched condition are presented in Fig. 2. It is evident that polygonal ferrite structures are formed in all the three steels. The grain sizes of the 0Al, 0.5Al, and 1Al steels are determined to be 61 ± 8, 59 ± 6, and 56 ± 15 μm, respectively, indicating that the Al additions have no significant effect on the grain size of the Fe-Cu-based steels. In the following, we select the 0Al and 1Al steels as model materials and comparatively characterize their microstructures at the atomic- and nano-scale.

The temporal evolution of precipitate microstructures of the 0Al and 1Al steels were investigated by APT. Figure 3 illustrates the APT reconstruction of the 0Al and 1Al steels in the 15-min and 1-h aged conditions at 550 °C. The 10 at.% Cu iso-concentration surfaces were used to visualize the Cu-rich nanoclusters. It is evident that spheroidal Cu-rich nanoclusters are uniformly distributed in the matrix in both steels. The average radius, number density, and

volume fraction of Cu-rich nanoclusters in the 0Al and 1Al steels in the 15-min and 1-h aged conditions are displayed in Fig. 4. For the 0Al steel, the average radius of Cu-rich nanoclusters increases from 1.44 ± 0.52 nm in 15-min aged condition to 2.17 ± 0.55 nm in 1-h aged condition, whereas the number density decreases from 1.2×10^{24} m^{-3} in 15-min aged condition to 5.0×10^{23} m^{-3} in 1-h aged condition. The volume fraction of Cu-rich nanoclusters increases from 1.5% ± 0.4% in the 15-min condition to 2.1% ± 0.3% in the 1-h condition. After adding 1 wt.% Al, the average radius of Cu-rich nanoclusters increases from 1.13 ± 0.36 nm in the 15-min aged condition to 2.23 ± 0.67 nm in 1-h aged condition, whereas the number density decreases from 1.6×10^{24} m^{-3} in 15-min aged condition to 3.6×10^{23} m^{-3} in 1-h aged condition. The volume fraction of Cu-rich nanoclusters increases from 1.0% ± 0.3% in the 15-min condition to 1.7% ± 0.3% in the 1-h condition. From the above statistical data, the volume fraction of Cu-rich nanoclusters in the 0Al steel is lightly lower than that in the 1Al steel (Fig. 4c), especially in the early stage of precipitation, suggesting that Al is likely to inhibit the precipitation of Cu-rich nanoclusters.

1-nm-thick atom maps through the centers of the Cu-rich nanoclusters in the 0Al and 1Al steels in the two aged conditions are shown in Fig. 5, in which the relative positions and extents of the Cu (green) and Al (red) atoms are indicated. It is evident that the enrichment of Cu increases with increasing aging time in both steels. More intriguingly, Al exhibits an obvious segregation to the Cu-rich nanocluster core. To get more precise information about the partitioning behavior of Al and its influence on the precipitate composition, proximity histograms of Cu-rich nanoclusters in the 0Al and 1Al steels are displayed in Fig. 6. For the 0Al steel, the concentration of Cu in the Cu-rich nanocluster core increases from 75.2 ± 4.7 at.% in the 15-min condition to 88.8 ± 3.0 at.% in the 1-h condition, whereas that of Fe decreases from 24.8 ± 4.7 at.% in the 15-min condition to 11.2 ± 3.0 at.% in the 1-h condition. For the 1Al steel, although the trend of the variation of the Cu and Fe concentration profiles is similar

to that of the 0Al steel, the concentration of Cu and Fe in the Cu-rich nanoclusters is slightly lower than that in the 0Al steel in the same conditions. Notably, a considerable amount of Al partitions to the Cu-rich nanocluster core in both conditions studied. The concentrations of Al in the Cu-rich nanocluster core in the 15-min and 1-h conditions are 5.0 ± 0.5 at.% and 5.5 ± 0.7 at.%, respectively, whereas those in the matrix in the 15-min and 1-h conditions are 2.2 ± 0.1 at.% and 2.2 ± 0.1 at.%, respectively. There is no apparent segregation of Al at the interface between the Cu-rich nanoclusters and matrix in both conditions studied. The above observations provide a compelling evidence for the intrinsic partitioning of Al to the Cu-rich nanoclusters.

To understand the influence of cluster size on the composition of Cu-rich nanoclusters, the composition of each individual nanocluster was analyzed. Figure 7 displays the Cu, Fe, and Al concentrations in the nanoclusters with different cluster sizes in the 15-min and 1-h aged conditions. In spite of some data scattering, there is a clear trend of increasing Cu concentration and decreasing Fe concentration with increasing cluster size. Specifically, as the cluster size increases from approximately 0.6 nm to 3.2 nm, the Cu concentration increases from approximately 25 at.% to 80 at.%, whereas the Fe concentration decreases from approximately 70 at.% to 20 at.%. In contrast, the Al concentration does not exhibit a significant variation with cluster size.

4. Discussion

4.1 Cluster size-dependent composition of Cu-rich nanoclusters

The APT results indicate that the Cu and Fe concentrations in the Cu-rich nanoclusters evolves with cluster size; this phenomenon has also been observed in previous studies of Fe-Cu-based alloys [21,38]. Basically, the compositional variations of precipitates can be influenced by the thermodynamic and kinetic properties of the precipitates. In this study,

several factors could possibly contribute to the compositional evolution of the Cu-rich nanoclusters. First, thermodynamic simulations suggested that at initial stages of precipitation, the incorporation of Fe into Cu-rich nanoclusters can lower the interfacial energy, resulting in a higher net driving force and therefore reduced activation energy for Cu-rich nanocluster nucleation [39]. As the Cu-rich nanoclusters grow, the relative influence of interfacial energy on the Gibbs free energy of nanoclusters becomes less pronounced because of an increasing relevance of bulk energy contribution. Thus, the Cu-rich nanoclusters are initially metastable with a high Fe concentration and their composition gradually evolves towards equilibrium as the nanoclusters grow. Second, kinetic considerations are another possible source of the compositional evolution of the Cu-rich nanoclusters [40]. Perhaps there is not enough time for diffusion to establish the equilibrium composition in fine clusters at early stages of precipitation, and thus, the Cu and Fe concentrations in the Cu-rich nanoclusters would be expected to vary with aging time and cluster size. In addition, the diffusivity of Cu, Fe, and Al in the bcc Fe at 550 ^{o}C are 1.5×10^{-20}, 2.3×10^{-20}, and 5.7×10^{-19} m^2/s, respectively [41]. It is evident that the diffusion of Al in the bcc Fe is much faster than that of Cu in the bcc Fe. Thus, the Al concentration in the Cu-rich nanoclusters is less constrained by the kinetic factor, which could be a possible reason for the steady concentration of Al in the Cu-rich nanoclusters.

4.2 Al partitioning and its effects on Cu-rich nanocluster precipitation

The aforementioned APT results reveal that Al partitions to the Cu-rich nanoclusters, rather than the ferritic matrix or nanocluster/matrix interface; this is an intrinsic partitioning behavior of Al in the Cu-rich nanocluster-strengthened ferritic steels. To understand the underlying mechanism of the intrinsic partitioning behavior of Al in the Cu-rich nanocluster-strengthened steels, first-principles calculations were performed to determine the interactions of Al with the bcc-Cu and bcc-Fe phases in the Fe-Cu-Al system. To simulate the precipitation

of bcc Cu in bcc Fe, a 128-atom supercell containing a 16-atom bcc Cu core and a surrounding 112-atom bcc Fe was constructed. To study the substitutional energy of Al, one Fe or Cu atom at different positions was substituted by one Al atom. The substitutional energy of Al in the 128-atom supercells was calculated by the following equations:

$$E_{Al\to Fe} = \left[\left(E^{total}_{Fe_{111}Cu_{16}Al_1} + \mu_{Fe}\right) - \left(E^{total}_{Fe_{112}Cu_{16}} + \mu_{Al}\right)\right] / n_{Al} \quad (1)$$

$$E_{Al\to Cu} = \left[\left(E^{total}_{Fe_{112}Cu_{15}Al_1} + \mu_{Cu}\right) - \left(E^{total}_{Fe_{112}Cu_{16}} + \mu_{Al}\right)\right] / n_{Al} \quad (2)$$

where $E^{total}_{Fe_{111}Cu_{16}Al_1}$, $E^{total}_{Fe_{112}Cu_{15}Al_1}$, and $E^{total}_{Fe_{112}Cu_{16}}$ are the total energies of the 128-atom supercells with the substitution of Al for Fe, with the substitution for Cu, and without Al substitution, respectively, μ_{Fe}, μ_{Cu}, and μ_{Al} are the chemical potentials of Fe, Cu, and Al, respectively, n_{Al} = 1 is the number of Al atom in the calculation. The substitutional energies of the two types of models were calculated and are given in Fig. 8. The average substitutional energies of Al for Fe and Cu are determined to be -0.60 ± 0.29 eV and -1.11 ± 0.17 eV, respectively. The substitutional energy of Al in bcc Cu is more negative than that in bcc Fe, which implies that the Al substitution in bcc Cu is more energetically favorable as compared with that in bcc Fe. Therefore, Al is energetically favorable to partition to the Cu-rich nanoclusters, forming the Cu/Al-enriched nanoclusters in the Fe-Cu-Al steels.

We now discuss the effect of Al partitioning on the precipitation behavior of Cu-rich nanoclusters in steels. According to the classical nucleation theory, the nucleation rate of precipitates is closely related to the chemical driving force, interfacial energy, and strain energy for nucleation [42]. The critical nucleation energy can be described by [42]

$$\Delta G = \frac{16\pi\gamma^3}{3\left(\Delta G_v - \Delta G_\varepsilon\right)^2} \quad (3)$$

where ΔG is the critical energy for nucleation, ΔG_v is the chemical driving force, γ is the interfacial energy for nucleation, and ΔG_ε is the strain energy. In the following, the influence of Al partitioning on the three terms related to the nucleation of Cu-rich nanoclusters is analyzed. First, the attractive interaction of Cu−Cu pairs provides a chemical driving force for Cu precipitation. We performed first-principles calculations to investigate the effect of Al on the formation energy of Cu-Cu pairs. To consider the influence of the number of Cu−Cu pairs in the calculation, we constructed two 54-atom supercells containing one and two Cu-Cu pairs on the basis of a bcc-Fe lattice, in which the Cu atoms have the first nearest-neighbor relationship. To investigate the interaction of Al with the Cu-Cu pairs, one Fe atom at the first nearest-neighbor position of the Cu-Cu pairs was substituted by one Al atom. For comparison, the models with Al occupying a site that is far away from the Cu-Cu pairs (i.e., at the fifth nearest-neighbor site) were constructed. In these models, the formation energy of the Cu-Cu pair can be calculated by

$$E_{Cu-Cu} = E_{Fe_{53-n}Cu_nAl_1} + nE_{Fe_{54}} - nE_{Fe_{53}Cu_1} - E_{Fe_{53}Al_1} \quad (4)$$

where n is the number of Cu atoms, and $E_{Fe_{53-n}Cu_nAl_1}$, $E_{Fe_{54}}$, $E_{Fe_{53}Cu_1}$, and $E_{Fe_{53}Al_1}$ represent the total energy of the $Fe_{53-n}Cu_nAl_1$, Fe_{54}, $Fe_{53}Cu_1$, and $Fe_{53}Al_1$ supercells, respectively. The calculated energies of the models with different sites of Al substitution are displayed in Fig. 9. The Al atom at the fifth nearest-neighbor site is far away from the Cu-Cu pairs, and there would be very weak or negligible interaction between the Al atom and Cu-Cu pairs. Thus, the formation energy of the Cu-Cu pairs in the model with Al occupying the fifth nearest-neighbor site can be used as a reference that represents a weak interaction between the Al atom and the Cu-Cu pairs. In the models with one Cu-Cu pair, the formation energy of the Cu-Cu pair with Al occupying the first nearest-neighbor site is similar to that with Al occupying the fifth nearest-neighbor site, suggesting that Al at both sites has negligible interaction with the Cu-Cu

pair. A similar observation can be made in the models with two Cu-Cu pairs. The above calculation results indicate that Al has a negligible influence on the formation energy of Cu-Cu pairs. In other words, Al has no significant effect on the chemical driving force for the formation of Cu-rich nanoclusters. Second, the interfacial energy term is related to the interface chemistry, which can be influenced by interfacial segregation [43,44]. In this study, the APT results reveal that Al partitions to the precipitate core, rather than the Cu-cluster/matrix interface. In addition, Al does not induce an obvious change of the interface chemistry. Therefore, it appears that the Al partitioning has no significant influence on the interfacial energy of Cu-rich nanoclusters. Third, the strain energy term is influenced by the lattice mismatch between the Cu-rich nanoclusters and matrix. Because the atomic radius of Cu (1.28 Å) is larger than that of Fe (1.24 Å) [25], the formation of Cu-rich nanoclusters would create a positive elastic misfit strain at the interface. The APT results indicate that Al partitions to the Cu-rich nanoclusters and substitutes for 5-6 at.% Cu. Because the atomic radius of Al (1.43 Å) is larger than that of Cu (1.28 Å) and Fe (1.24 Å) [25], the partial substitution of Al for Cu should result in an increase in the lattice constant of the Cu-rich nanoclusters and hence enlarge the lattice misfit between the Cu-rich nanoclusters and α-Fe matrix. Thus, the Al partitioning increases the strain energy for the nucleation of Cu-rich nanoclusters, leading to a slight decrease of the nucleation rate of the nanoclusters. As a result, the volume fraction of Cu-rich nanoclusters in the 1Al steel is slightly lower than that in the 0Al steel (cf. Fig. 4).

Therefore, it was demonstrated that Al is intrinsically favorable to partition to the Cu-rich nanocluster core. This partitioning behavior is different from that in multicomponent steels with the co-existence of Ni and Al, in which both Ni and Al segregate to the interface between the Cu-rich nanoclusters and matrix. It is likely that in the case of Fe-Cu-Ni-Al-based steels, the partitioning of Al to the interface is influenced by the interfacial segregation of Ni due to

the strong affinity of Al to Ni. This finding may be useful in controlling the precipitation behavior of Cu-rich nanoclusters in ferritic steels for industrial applications.

4.3 Strengthening mechanism

To gain a fundamental insight into the relationship between the precipitate microstructure and mechanical properties of the Al-free and Al-containing steels, we model the strengthening mechanisms of the Cu-rich nanoclusters in the 0Al and 1Al steels. Cu-rich nanoclusters are known to be weak obstacles and sheared by dislocations in Fe-based alloys [19]. The degree of precipitation strengthening is highly dependent on the precipitate microstructure, particularly the combined effect of cluster size and inter-cluster spacing, which can be decribed by [45]:

$$\Delta\sigma = \frac{M\gamma R}{bL}, \tag{5}$$

where $M = 3$ is the Taylor factor for bcc metals, $\gamma = 0.37$ J/m^2 is the surface energy of Cu-rich nanoclusters [46], R is the average cluster radius, $b = 0.25$ nm is the Burgers vector, and L is the mean inter-cluster spacing, which can be calculated by [47]

$$L = 0.866 \times \left(RN\right)^{-1/2}, \tag{6}$$

where N is the number density of Cu-rich nanoclusters. With the inputs of the radius and number density of Cu-rich nanoclusters determined by APT in each condition, the theoretical strength increments can be determined. According to an empirical relationship between yield strength and Vickers hardness for bcc steels, i.e., $\Delta H = 1/3\Delta\sigma$ [48], the theoretical hardness increment in each condition was estimated, and the results are summarized in Table 1. It is seen that the theoretical values of hardness increment due to precipitation hardening are in good agreement with the experimental results within experimental uncertainties. In addition, it is

noted that although the 0Al and 1Al steels have significantly different precipitate microstructures, the precipitation hardening response of the two steels are pretty similar in the two aged conditions, which indicates that the degree of precipitation strengthening depends majorly on the combined effect of cluster size and inter-cluster spacing.

5. Conclusions

Through the combination of APT characterization and first-principles calculations, the intrinsic partitioning of Al and its influence on the nanoscale precipitation of Fe-Cu-based alloys were systematically studied. The APT results reveal that the Cu concentration increases and the Fe concentration decreases with increasing aging time and cluster size. Moreover, Al partitions to the Cu-rich nanoclusters with a concentration of 5-6 at.%, which is accompanied by a slight decrease in the volume fraction of Cu-rich nanoclusters. The first-principles calculations indicate that the Al substitution in bcc Cu is more energetically favorable as compared with that in bcc Fe. The partial substitution of Al for Cu has no significant influence on the chemical driving force and interfacial energy but slightly increases the strain energy due to the large atomic size of Al, which slightly inhibits the precipitation of Cu-rich nanoclusters. As a result, the volume fraction of Cu-rich nanoclusters in the Al-containing steels is slightly lower than that in the Al-free steels. In addition, the effects of Al on the precipitation strengthening response were quantitatively evaluated, and the results indicate that the degree of precipitation strengthening depends majorly on the combined effect of cluster size and inter-cluster spacing.

Acknowledgements

This research was supported by the National Natural Science Foundation of China (51801169), Shenzhen Science and Technology Program (JCYJ20210324142203009), State Key Laboratory for Advanced Metals and Materials Open Fund (2017-ZD01 and 2017-Z07),

Guangzhou International Science & Technology Cooperation Program (201907010026), Chinese National Engineering Research Centre for Steel Construction (Hong Kong Branch) at PolyU (P0013862), and the key program in the Youth Elite Support plan in Universities of Anhui Province (gxyqZD2016318).

Data availability

The data that support the findings of this study are available from the corresponding author on reasonable request.

References

[1] Q.D. Liu, H. Song, J. Zhang, J.X. Ding, Y.H. Chen, J.F. Gu, Strengthening of Ni-Mn-Cu-Al-Co steel by nanoscale Cu and β-NiAl co-precipitated couples, Mater. Charact. 171 (2021) 110754.

[2] J.H. Gao, S.H. Jiang, H.R. Zhang, Y.H. Huang, D.K. Guan, Y.D. Xu, S.K. Guan, L.A. Bendersky, A.V. Davydov, Y. Wu, H.H. Zhu, Y.D. Wang, Z.P. Lu, W.M. Rainforth, Facile route to bulk ultrafine-grain steels for high strength and ductility, Nature 590.7845 (2021) 262-267.

[3] M. Kapoor, D. Isheim, G. Ghosh, S. Vaynman, M.E. Fine, Y.W. Chung, Aging characteristics and mechanical properties of 1600 MPa body-centered cubic Cu and B2-NiAl precipitation-strengthened ferritic steel, Acta Mater. 73 (2014) 56-74.

[4] D. Isheim, M.S. Gagliano, M.E. Fine, D.N. Seidman, Interfacial segregation at Cu-rich precipitates in a high-strength low-carbon steel studied on a sub-nanometer scale, Acta Mater. 54.3 (2006) 841-849.

[5] W. Hou, Q.D. Liu, J.F. Gu, Improved impact toughness by multi-step heat treatment in a 1400 MPa low carbon precipitation-strengthened steel, Mater. Sci. Eng. A 797 (2020) 140077.

[6] D.Y. Huang, J.C. Yan, X.W. Zuo, Co-precipitation kinetics, microstructural evolution and interfacial segregation in multicomponent nano-precipitated steels, Mater. Charact. 155 (2019) 109786.

[7] D. Jain, D. Isheim, A.H. Hunter, D.N. Seidman, Multicomponent high-strength low-alloy steel precipitation-strengthened by sub-nanometric Cu precipitates and M_2C carbides, Metall. Mater. Trans. A 47.8 (2016) 3860-3872.

[8] D. Görzen, H. Schwich, B. Blinn, W.W. Song, U. Krupp, W. Bleck, T. Beck, Influence of

Cu precipitates and C content on the defect tolerance of steels, Int. J. Fatigue 144 (2021) 106042.
[9] K. Sawada, K. Sekido, M. Murata, K. Kamihira, K. Kimura, Precipitation behavior during aging and creep in 18Cr-9Ni-3Cu-Nb-N steel, Mater. Charact. 141 (2018) 279-285.
[10] M.K. Jiang, Y. Han, T. Zhang, J.P. Sun, G.Q. Zu, H. Chen, X. Ran, Microstructural characterization of aging precipitation behavior of 17Cr-0.86Si-1.2Cu-0.5Nb ferritic stainless steel, Mater. Charact. 171 (2021)110779.
[11] B.B. Zhao, J.F. Fan, Z. Chen, X.P. Dong, F. Sun, L.T. Zhang, Evolution of precipitates in a Cu-containing alumina-forming austenitic steel after short-term mechanical tests, Mater. Charact. 125 (2017) 37-45.
[12] G. Han, Z.J. Xie, Z.Y. Li, B. Lei, C.J. Shang, R.D.K. Misra, Evolution of crystal structure of Cu precipitates in a low carbon steel, Mater. Des. 135 (2017) 92-101.
[13] P.J. Othen, M.L. Jenkins, G.D.W. Smith, W.J. Phythian, Transmission electron microscope investigations of the structure of copper precipitates in thermally-aged Fe-Cu and Fe-Cu-Ni, Philos. Mag. Lett. 64.6 (1991) 383-391.
[14] S.R. Goodman, S.S. Brenner, J.R. Low, An FIM-atom probe study of the precipitation of copper from Iron-1.4 at. Pct copper. Part II: Atom probe analyses, Metall. Trans. 4.10 (1973) 2371-2378.
[15] D. Isheim, M.S. Gagliano, M.E. Fine, D.N. Seidman, Interfacial segregation at Cu-rich precipitates in a high-strength low-carbon steel studied on a sub-nanometer scale, Acta Mater. 54.3 (2006) 841-849.
[16] Z.W. Zhang, C.T. Liu, X. L. Wang, K.C. Littrell, M.K. Miller, K. An, B.A. Chin, From embryos to precipitates: A study of nucleation and growth in a multicomponent ferritic steel, Phys. Rev. B 84.17 (2011) 174114.
[17] H. J. Pan, H. Ding, M.H. Cai, D. Kibaroglu, Y. Ma, W.W. Song, Precipitation behavior and austenite stability of Nb or Nb–Mo micro-alloyed warm-rolled medium-Mn steels, Mater. Sci. Eng. A 766 (2019) 138371.
[18] O.I. Gorbatov, Y.N. Gornostyrev, P.A. Korzhavyi, A.V. Ruban, Effect of Ni and Mn on the formation of Cu precipitates in α-Fe, Scr. Mater. 102 (2015) 11-14.
[19] Z.B. Jiao, J.H. Luan, Z.W. Zhang, M.K. Miller, W.B. Ma, C.T. Liu, Synergistic effects of Cu and Ni on nanoscale precipitation and mechanical properties of high-strength steels, Acta Mater. 61.16 (2013) 5996-6005.
[20] Y.R. Wen, A. Hirata, Z.W. Zhang, T. Fujita, C.T. Liu, J. H. Jiang, M.W. Chen,

Microstructure characterization of Cu-rich nanoprecipitates in a Fe–2.5 Cu–1.5 Mn–4.0 Ni–1.0 Al multicomponent ferritic alloy, Acta Mater. 61.6 (2013) 2133-2147.
[21] R.P. Kolli, D.N. Seidman, The temporal evolution of the decomposition of a concentrated multicomponent Fe–Cu-based steel, Acta Mater. 56.9 (2008) 2073-2088.
[22] Q.D. Liu, J.F. Gu, W.Q. Liu, On the role of Ni in Cu precipitation in multicomponent steels, Metall. Mater. Trans. A 44.10 (2013) 4434-4439.
[23] M. Kapoor, D. Isheim, S. Vaynman, M.E. Fine, Y.W. Chung, Effects of increased alloying element content on NiAl-type precipitate formation, loading rate sensitivity, and ductility of Cu- and NiAl-precipitation-strengthened ferritic steels, Acta Mater. 104 (2016) 166-171.
[24] Z.B. Jiao, J.H. Luan, M.K. Miller, C.T. Liu, Precipitation mechanism and mechanical properties of an ultra-high strength steel hardened by nanoscale NiAl and Cu particles, Acta Mater. 97 (2015) 58-67.
[25] A. Takeuchi, A. Inoue, Classification of bulk metallic glasses by atomic size difference, heat of mixing and period of constituent elements and its application to characterization of the main alloying element, Mater. Trans. 46.12 (2005) 2817-2829.
[26] Y.P. Xie, S.J. Zhao, First principles study of Al and Ni segregation to the α-Fe/Cu (1 0 0) coherent interface and their effects on the interfacial cohesion, Comput. Mater. Sci. 63 (2012) 329-335.
[27] S.H. Jiang, X.Q. Xu, W. Li, B. Peng, Y. Wu, X.J. Liu, H. Wang, X.Z. Wang, Z.P. Lu, Strain hardening mediated by coherent nanoprecipitates in ultrahigh-strength steels, Acta Mater. (2021) 116984.
[28] H. Guo, M. Enomoto, C.J. Shang, Simulation of bcc-Cu precipitation in ternary Fe-Cu-M alloys, Comput. Mater. Sci. 141 (2018) 101-113.
[29] J.L. Wang, M. Enomoto, C.J. Shang, First-principles study on the interfacial segregation at coherent Cu precipitate/Fe matrix interface, Scr. Mater. 185 (2020) 42-46.
[30] X.Y. Gao, H.Y. Wang, C. Ma, L. Xing, H.P. Ren, Study on the Partitioning of Alloying Elements Between bcc-Fe Matrix and bcc-Cu Precipitates and the Corresponding Effects on the Precipitation Interface, Metall. Mater. Trans. A 51.10 (2020) 5444-5452.
[31] H.Y. Wang, X.Y. Gao, S.M. Chen, Y.M. Li, Z.W. Wu, H.P. Ren, Effects of Al on the precipitation of B2 Cu-rich particles in Fe–Cu ferritic alloy: Experimental and theoretical study, J. Alloys Compd. 846 (2020) 156386.
[32] C. Drouven, W.W. Song, W. Bleck, Phase-Specific Precipitation of Intermetallic Phases in Fe Al Mn Ni C Duplex Steels, Steel Res. Int. 90.1 (2019) 1800440.
[33] S.A. Briggs, P.D. Edmondson, K.C. Littrell, Y. Yamamoto, R.H. Howard, C.R. Daily, K.A.

Terrani, K. Sridharan, K.G. Field, A combined APT and SANS investigation of α′ phase precipitation in neutron-irradiated model FeCrAl alloys, Acta Mater. 129 (2017) 217-228.
[34] C.H. Kuo, B. Shassere, J. Poplawsky, Y. Yamamoto, S.S. Babu, Validation of an alloy design strategy for stable Fe–Cr–Al–Nb-X ferritic alloys using electron microscopy and atom probe tomography, Mater. Charact. 158 (2019) 109987.
[35] G. Kresse, J. Hafner, Ab initio molecular-dynamics simulation of the liquid-metal–amorphous-semiconductor transition in germanium, Phys. Rev. B 49.20 (1994) 14251.
[36] G. Kresse, J. Furthmüller, Efficient iterative schemes for ab initio total-energy calculations using a plane-wave basis set, Phys. Rev. B 54.16 (1996) 11169.
[37] P. E. Blöchl, Projector augmented-wave method, Phys. Rev. B 50.24 (1994) 17953.
[38] M.D. Mulholland, D.N. Seidman, Nanoscale co-precipitation and mechanical properties of a high-strength low-carbon steel, Acta Mater. 59 (5) 1881-1897.
[39] E. Kozeschnik, Thermodynamic prediction of the equilibrium chemical composition of critical nuclei: Bcc Cu precipitation in α-Fe. Scripta Mater. 59 (9) 1018-1021.
[40] M. E. Fine, J.Z. Liu, M.D. Asta, An unsolved mystery: The composition of bcc Cu alloy precipitates in bcc Fe and steels. Mater. Sci. Eng. A 463. 1-2 (2007) 271-274.
[41] W. F. Gale, T.C. Totemeier, Smithells metals reference book, Elsevier, 2003.
[42] H.I. Aaronson, F.K. Legoues, An assessment of studies on homogeneous diffusional nucleation kinetics in binary metallic alloys, Metal. Tans. A 23.7 (1992) 1915-1945.
[43] D. Raabe, S. Sandlöbes, J. Millán, D. Ponge, H. Assadi, M. Herbig, P.P. Choi, Segregation engineering enables nanoscale martensite to austenite phase transformation at grain boundaries: A pathway to ductile martensite, Acta Mater. 61.16 (2013) 6132-6152.
[44] A. Biswas, D.J. Siegel, D.N. Seidman, Simultaneous Segregation at Coherent and Semicoherent Heterophase Interfaces, Phys. Rev. Lett. 105.7 (2010) 076102.
[45] R.W. Cahn, P. Haasen, Physical Metallurgy, North-Holland, Oxford, 1996.
[46] Z.W. Zhang, C.T. Liu, M.K. Miller, X.L. Wang, Y.R. Wen, T. Fujita, A. Hirata, M.W. Chen, G. Chen, B.A. Chin, A nanoscale co-precipitation approach for property enhancement of Fe-base alloys, Sci. Rep. 3.1 (2013) 1-6.
[47] A. Kelly, R.B. Nicholson, Strengthening methods in crystals, Elsevier, London, 1971.
[48] P. Zhang, S.X. Li, Z.F. Zhang, General relationship between strength and hardness, Mater. Sci. Eng. A 529 (2011) 62-73.

Figure Captions

Fig. 1. Hardness profiles of the 0Al, 0.5Al, and 1Al steels as a function of aging time.

Fig. 2. Microstructures of the (a) 0Al, (b) 0.5Al, and (c) 1Al steels in the as-quenched condition.

Fig. 3. APT characterization of the 0Al and 1Al steels in different aging conditions: (a) 0Al, 15 min, (b) 0Al, 1 h, (c) 1Al, 15 min, and (d) 1Al, 1 h.

Fig. 4. (a) Cluster radii, (b) number densities, and (c) volume fractions of Cu-rich nanoclusters of the 0Al and 1Al steels as a function of aging time.

Fig. 5. 1-nm-thick atom maps through representative Cu-rich nanoclusters in different conditions: (a) 0Al, 15 min, (b) 0Al, 1 h, (c) 1Al, 15 min, and (d) 1Al, 1 h.

Fig. 6. Proximity histograms of Cu-rich nanoclusters in different conditions: (a) 0Al, 15 min, (b) 0Al, 1 h, (c) 1Al, 15 min, and (d) 1Al, 1 h.

Fig. 7. Cu, Fe, and Al concentrations in the Cu-rich nanoclusters with different cluster sizes in the 15-min and 1-h aged conditions.

Fig. 8. Calculated substitutional energies of the structures with Al substitution for Fe and Cu.

Fig. 9. First-principles calculations of the formation energies of Cu-Cu pairs in the supercells with Al at the 1^{st}- and 5^{th}-nearest-neighbor (NN) sites.

Fig. 1

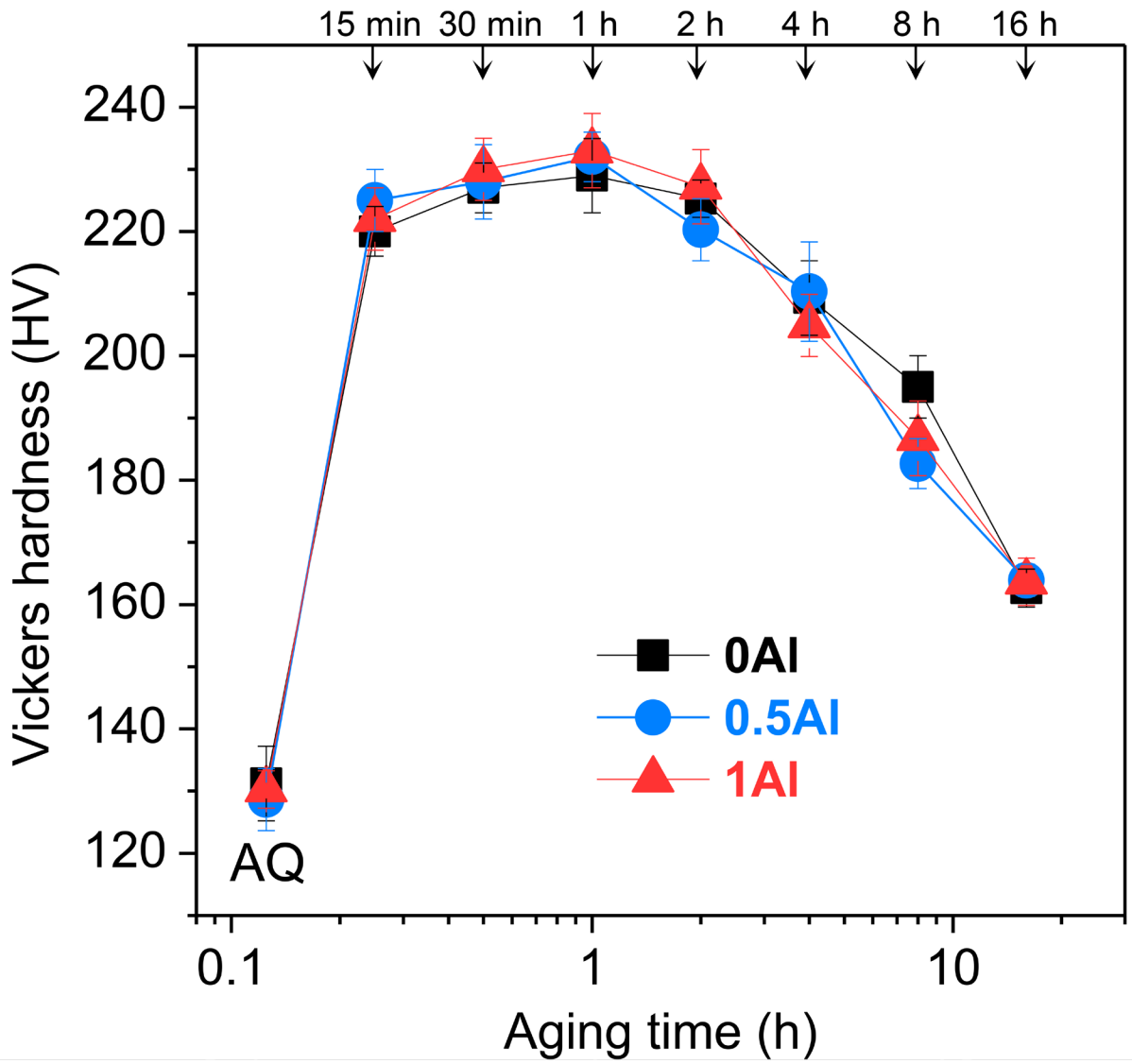
15 min
30 min
1 h
2 h
4 h
8 h
16 h
240
220
200
180
160
140
120
Vickers hardness (HV)
AQ
0.1
1
10
Aging time (h)
0Al
0.5Al
1Al

Fig. 2

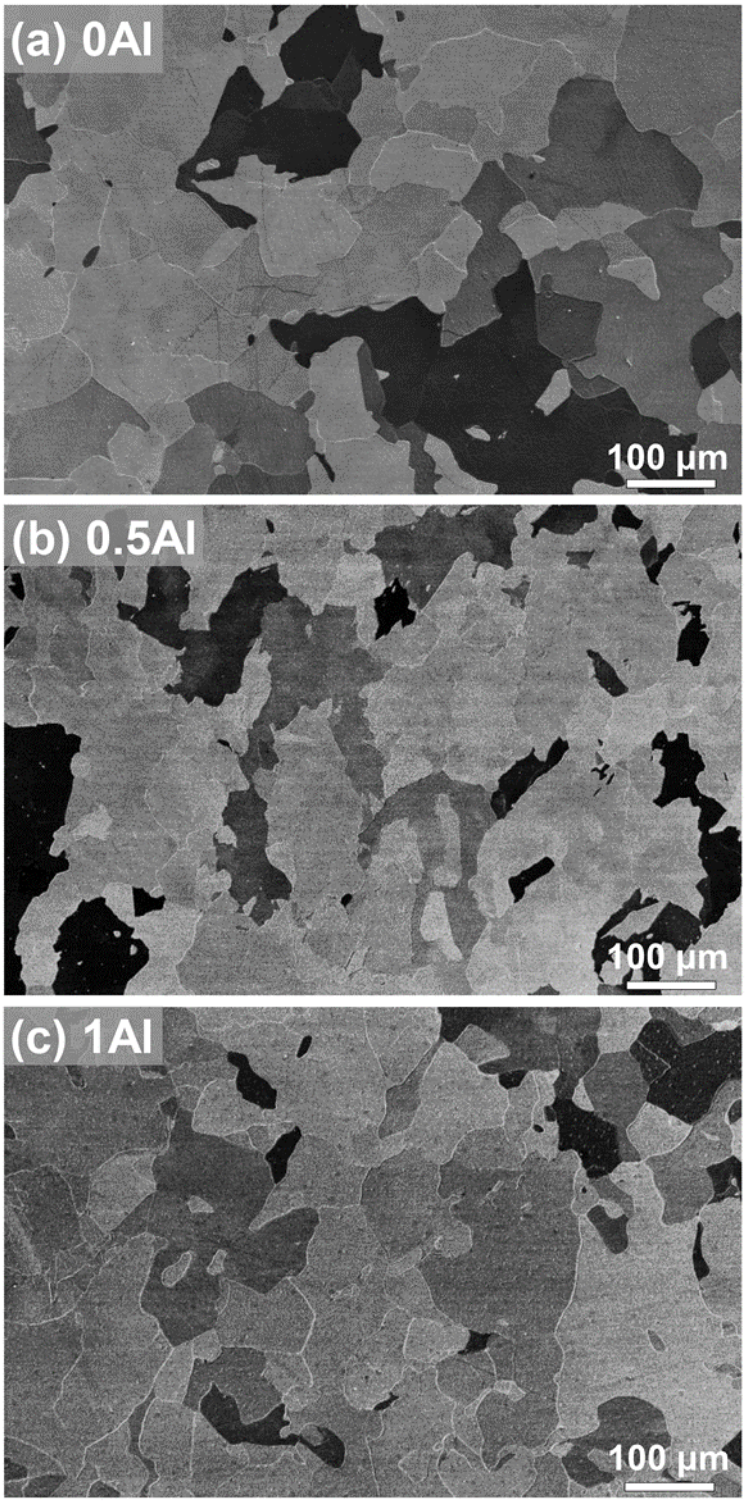

Fig. 3

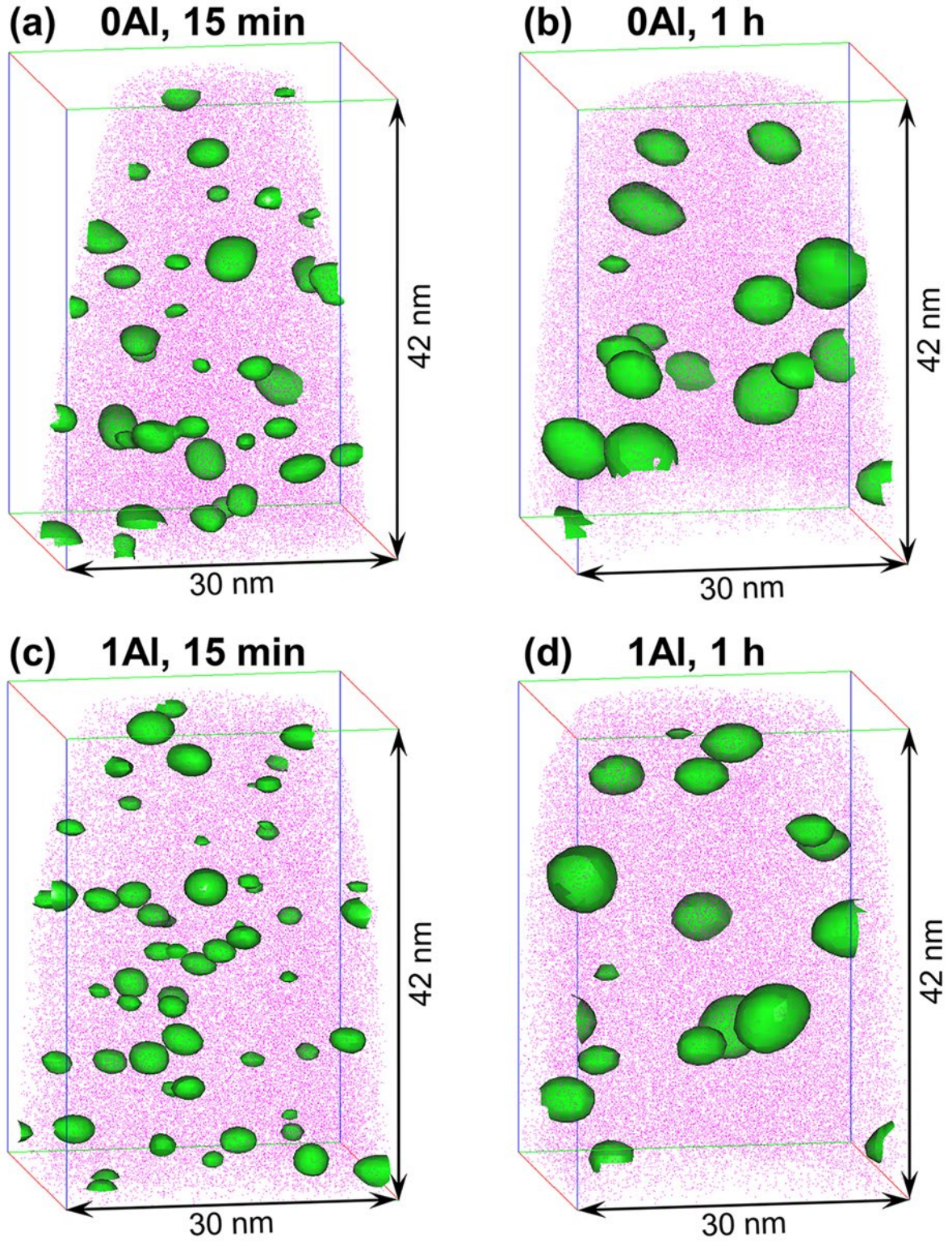
(a) 0Al, 15 min
42 nm
30 nm
(b) 0Al, 1 h
42 nm
30 nm
(c) 1Al, 15 min
42 nm
30 nm
(d) 1Al, 1 h
42 nm
30 nm

Fig. 4

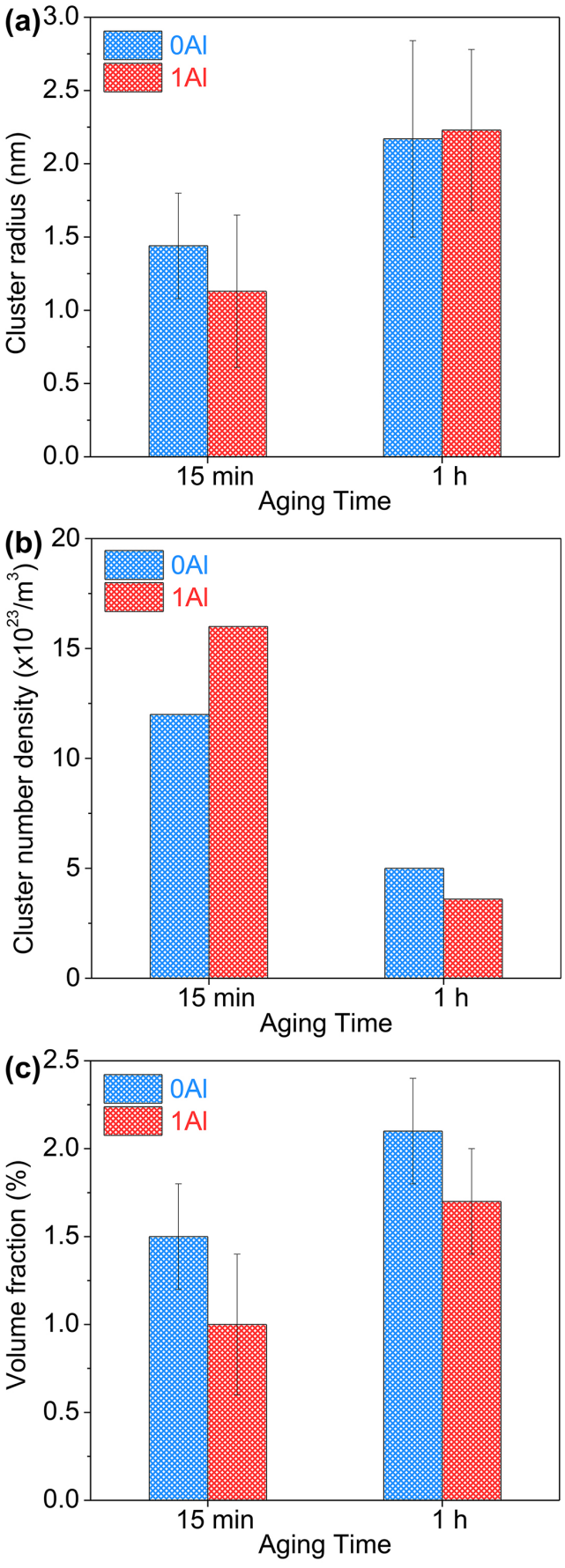
(a)
0Al
1Al
Cluster radius (nm)
3.0
2.5
2.0
1.5
1.0
0.5
0.0
15 min
1 h
Aging Time
(b)
0Al
1Al
Cluster number density (x10^23/m^3)
20
15
10
5
0
15 min
1 h
Aging Time
(c)
0Al
1Al
Volume fraction (%)
2.5
2.0
1.5
1.0
0.5
0.0
15 min
1 h
Aging Time

Fig. 5

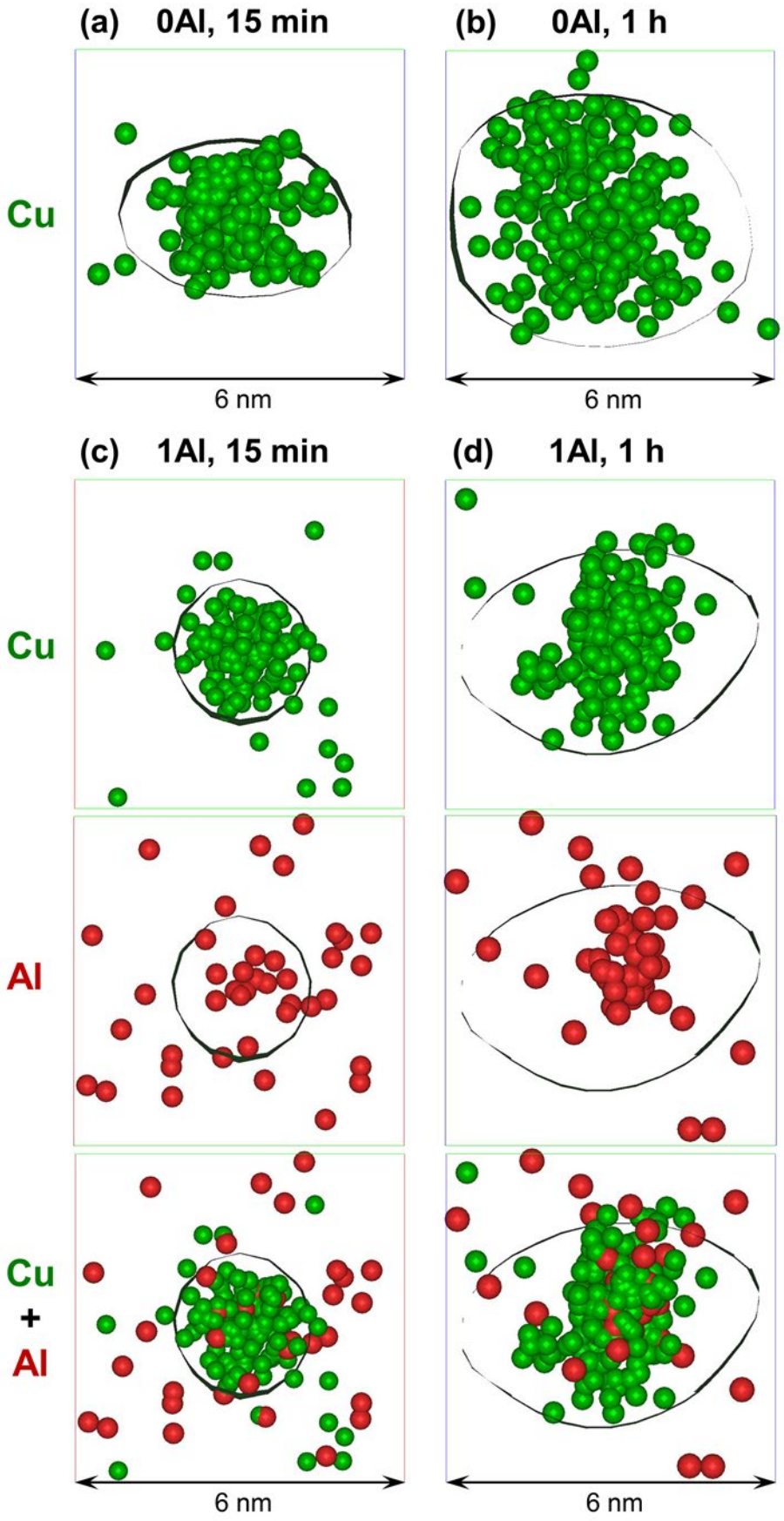
(a) 0Al, 15 min
(b) 0Al, 1 h
(c) 1Al, 15 min
(d) 1Al, 1 h
Cu
Cu
Al
Cu
+
Al
6 nm
6 nm
6 nm
6 nm

Fig. 6

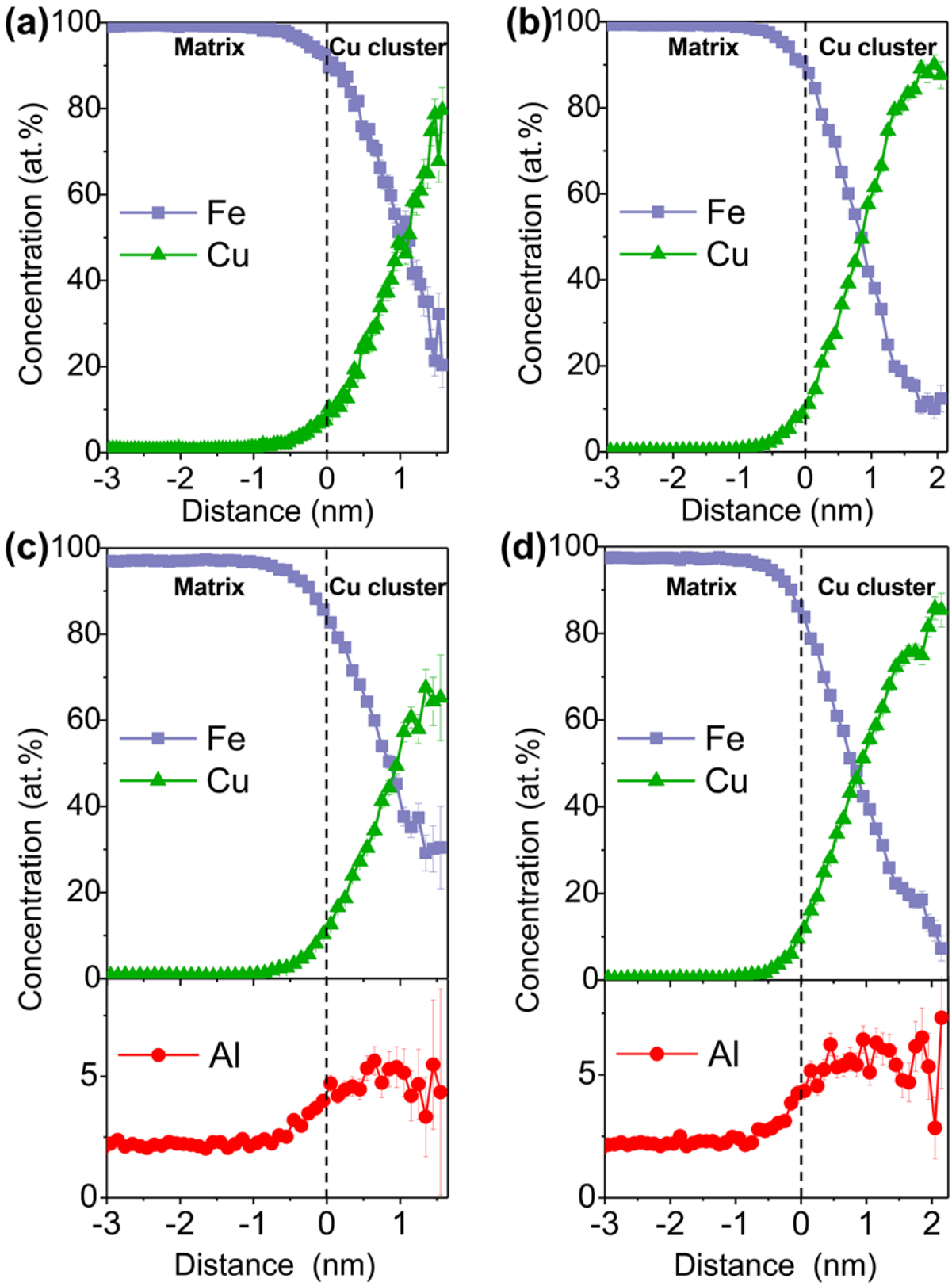
(a)
(b)
(c)
(d)
Matrix
Cu cluster
Fe
Cu
Al
Concentration (at.%)
Distance (nm)

Fig. 7

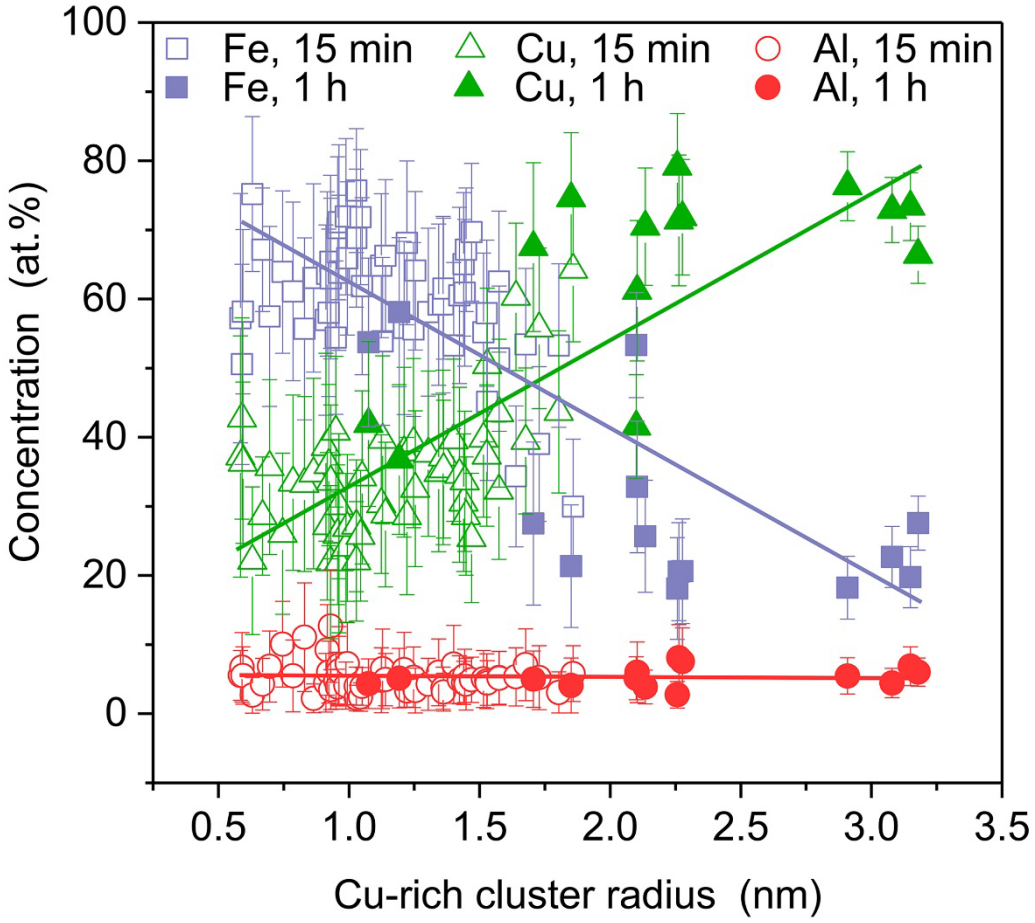
Fe, 15 min
Fe, 1 h
Cu, 15 min
Cu, 1 h
Al, 15 min
Al, 1 h
Concentration (at.%)
Cu-rich cluster radius (nm)
0
20
40
60
80
100
0.5
1.0
1.5
2.0
2.5
3.0
3.5

Fig. 8

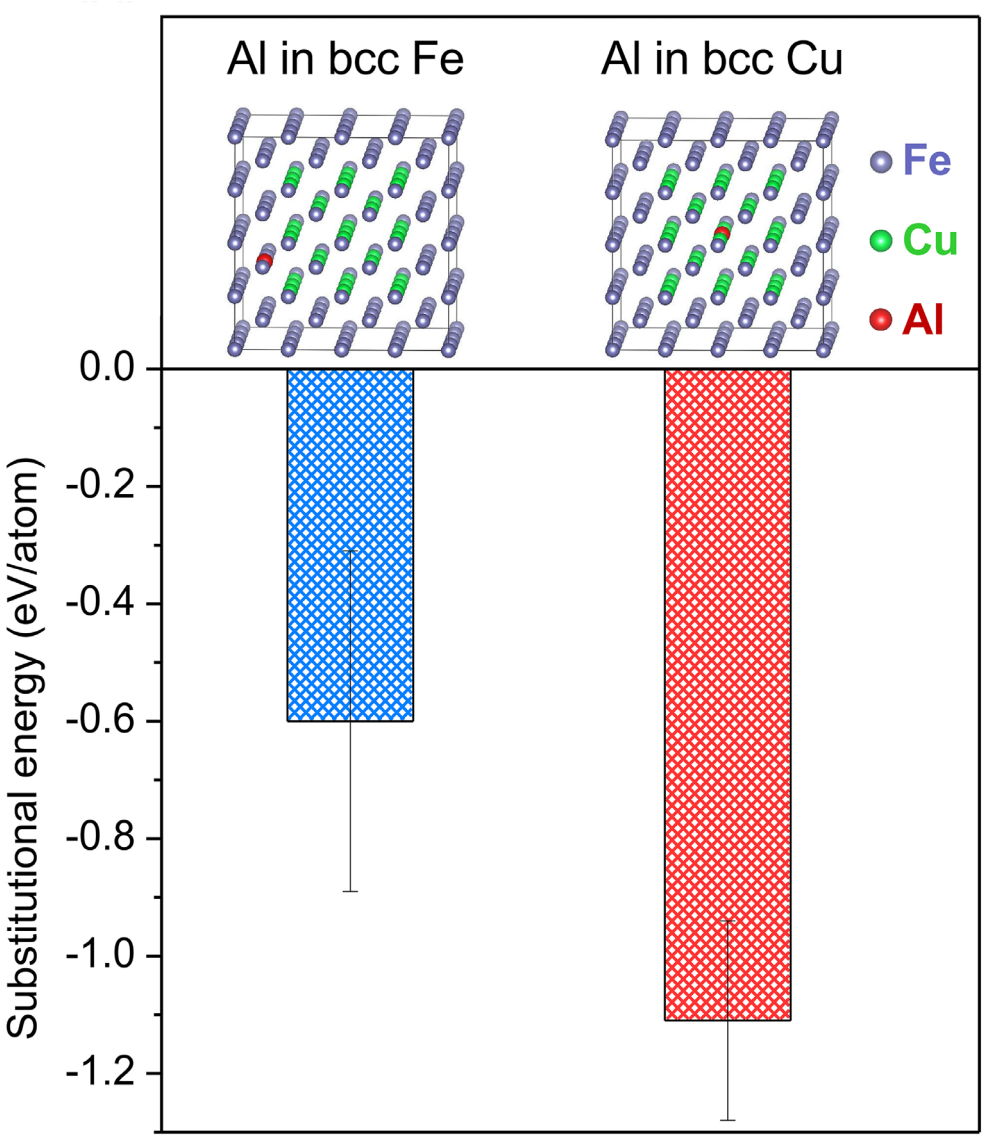
Al in bcc Fe
Al in bcc Cu
Fe
Cu
Al
0.0
-0.2
-0.4
-0.6
-0.8
-1.0
-1.2
Substitutional energy (eV/atom)

Fig. 9

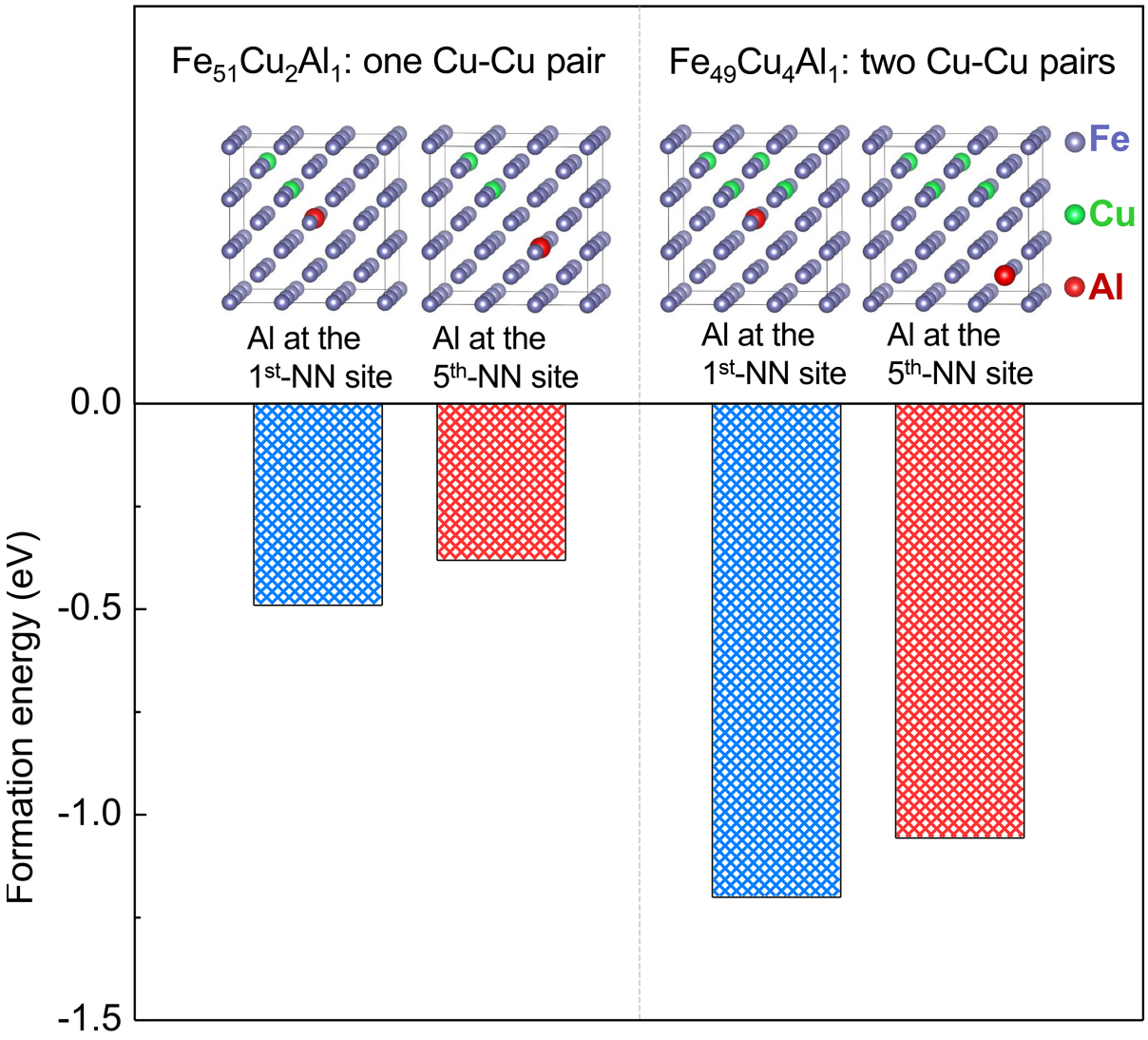
Fe51Cu2Al1: one Cu-Cu pair
Fe49Cu4Al1: two Cu-Cu pairs
Fe
Cu
Al
Al at the 1st-NN site
Al at the 5th-NN site
Al at the 1st-NN site
Al at the 5th-NN site
Formation energy (eV)
0.0
-0.5
-1.0
-1.5